

Article

3-Mercaptopropyl Trimethoxysilane @ Gadolinium Oxide Nanoprobes: An Effective Fluorescence-Sensing Platform for Cysteine

Sushil Kumar ¹, Ganga Ram Chaudhary ¹, Savita Chaudhary ^{1,*} and Ahmad Umar ^{2,3,*†}

¹ Department of Chemistry and Center of Advanced Studies in Chemistry, Panjab University, Chandigarh 160014, India

² Department of Chemistry, Faculty of Science and Arts, and Promising Centre for Sensors and Electronic Devices (PCSED), Najran University, Najran 11001, Saudi Arabia

³ Department of Materials Science and Engineering, The Ohio State University, Columbus, OH 43210, USA

* Correspondence: schaudhary@pu.ac.in (S.C.); ahmadumar786@gmail.com or umahmad@nu.edu.sa (A.U.)

† Adjunct Professor at the Department of Materials Science and Engineering, The Ohio State University, Columbus, OH 43210, USA.

Abstract: The current work aims to synthesize highly fluorescent and surface-functionalized gadolinium oxide nanoparticles (Gd_2O_3 NPs) with (3-mercaptopropyl) trimethoxysilane (MPTMS). The surface modification of Gd_2O_3 nanoparticles with MPTMS enhanced the stability and solubility of the nanoprobe in aqueous media. The size of the nanoprobe was controlled to 7 ± 1 nm using MPTMS coating. These valued points made the MPTMS@ Gd_2O_3 nanoparticles as economical, highly sensitive, selective nanoprobe with a quick response time for the detection of cysteine via the simple fluorescence-based methodology. The proposed strategy has offered the reliable detection of cysteine in the concentration range of $1\text{--}100 \mu\text{m}$ with a detection limit of 42 nm . The selective sensing of cysteine in human serum has jointly acknowledged the potential prospect of developing sensors in body fluids with great accuracy.

Keywords: Gd_2O_3 ; nanoparticles; fluorescence sensor; high performance



Citation: Kumar, S.; Chaudhary, G.R.; Chaudhary, S.; Umar, A.

3-Mercaptopropyl Trimethoxysilane @ Gadolinium Oxide Nanoprobes: An Effective Fluorescence-Sensing Platform for Cysteine. *Coatings* **2022**, *12*, 1636. <https://doi.org/10.3390/coatings12111636>

Academic Editor: Keith J. Stine

Received: 8 October 2022

Accepted: 26 October 2022

Published: 28 October 2022

Publisher's Note: MDPI stays neutral with regard to jurisdictional claims in published maps and institutional affiliations.



Copyright: © 2022 by the authors. Licensee MDPI, Basel, Switzerland. This article is an open access article distributed under the terms and conditions of the Creative Commons Attribution (CC BY) license (<https://creativecommons.org/licenses/by/4.0/>).

1. Introduction

The biologically active small thiols, such as cysteine (Cys), execute several biochemical activities, including fabrication of DNA, transmission of signals across the cells and protein folding in living beings [1–4]. The enzymatic posttranslational changes, bio-stimulations via catalysis, and detoxification of harmful toxins from living systems are also maintained by the application of Cys in human beings [4,5]. The prevailing anti-oxidative properties of Cys have made it an effective component for the entrapment of reactive oxygen species in the living system [6]. Around $240\text{--}300 \mu\text{m}$ concentration of Cys in human plasma is required for the proper functioning of biological processes [5]. Any kind of abnormality in Cys levels can lead to a series of disorders, including retarded growth in toddlers, damaging of skin and liver, depigmentation of hair, cardiovascular problems, tiredness, edema and decreasing levels of muscle and fat in the living system [4,7,8]. On the other hand, neurotoxicity has been observed due to the presence of excessive amounts of Cys in the living system [9]. Therefore, the accurate identification of Cys provides an effective way to treat several associated diseases via early diagnosis [4]. At present, different types of analytical methods, including chromatographic analysis, capillary electrophoresis, high-performance liquid chromatography (HPLC), and electrochemical- and colorimetric-based methods, have been utilized for the detection of Cys [7,10–13]. Among these methods, fluorescence-based methodology holds increasing interest because of its high selectivity, sensitivity with low cost easy processing and quick response time [14].

Up to now, a wide range of fluorescent probes and biosensors, including carbon dots, metal and their oxide/sulfide, organic and surface functionalized MOFs, have been designed for the accurate detection of Cys [1,14–17]. For instance, Raj and Sudarsanakumar have developed diosmin@silver NPs for the optical sensing of Cys [18]. Surface-functionalized CdS nanoparticles have been prepared for the fluorescence sensing of Cys with a 0.5–10 μm range [16]. N@CDs on Au NPs showed a quick response for Cys during colorimetric and photoluminescence analysis [19]. However, photochemical instability over a period with broad emission and narrow absorption bands with associated nanotoxicity has restricted its utilization in biological fluids [20].

Currently, Lanthanide oxide-based optical nanoprobes are identified as a budding celeb for the detection of trace levels of biologically active thiols [21]. The sharp emission, large Stokes and anti-Stokes shift, long fluorescence lifetime, and less autofluorescence [22–25] with controllable toxicity levels have further enhanced the potential scope of lanthanide oxide-based nanoprobes in applied and biomedical applications, including optical diodes, solar cells, lasers, photodynamic therapy, bio-photonics, drug delivery, optical bio-probes, and biolabeling markers [20,26–34]. Among the colossal range of lanthanide-based oxides, gadolinium oxide (Gd_2O_3) has been seen to be special due to its superior photochemical stability, long thermal stability and low phonon energy [35–37]. Their diagnostic and therapeutic properties have further makes Gd_2O_3 more efficient in bio-sensing [38,39]. Gd_2O_3 NPs exhibit a good emission profile with high charge transfer efficiency in the presence of analytes [40]. The optical properties of Gd_2O_3 NPs have reflected their diverse range of applications in luminescent devices, optical imaging and in targeting agent [41,42]. The facile synthesis, excellent characteristics, structure tailoring and functionalization with a targeting substance make Gd_2O_3 NPs a suitable candidate for detection of bio-molecules with great accuracy and sensitivity. Therefore, keeping the potential scope of Gd_2O_3 NPs, we hereby aimed to formulate a highly selective and sensitive fluorescent probe with Gd_2O_3 NPs, for the detection of Cys.

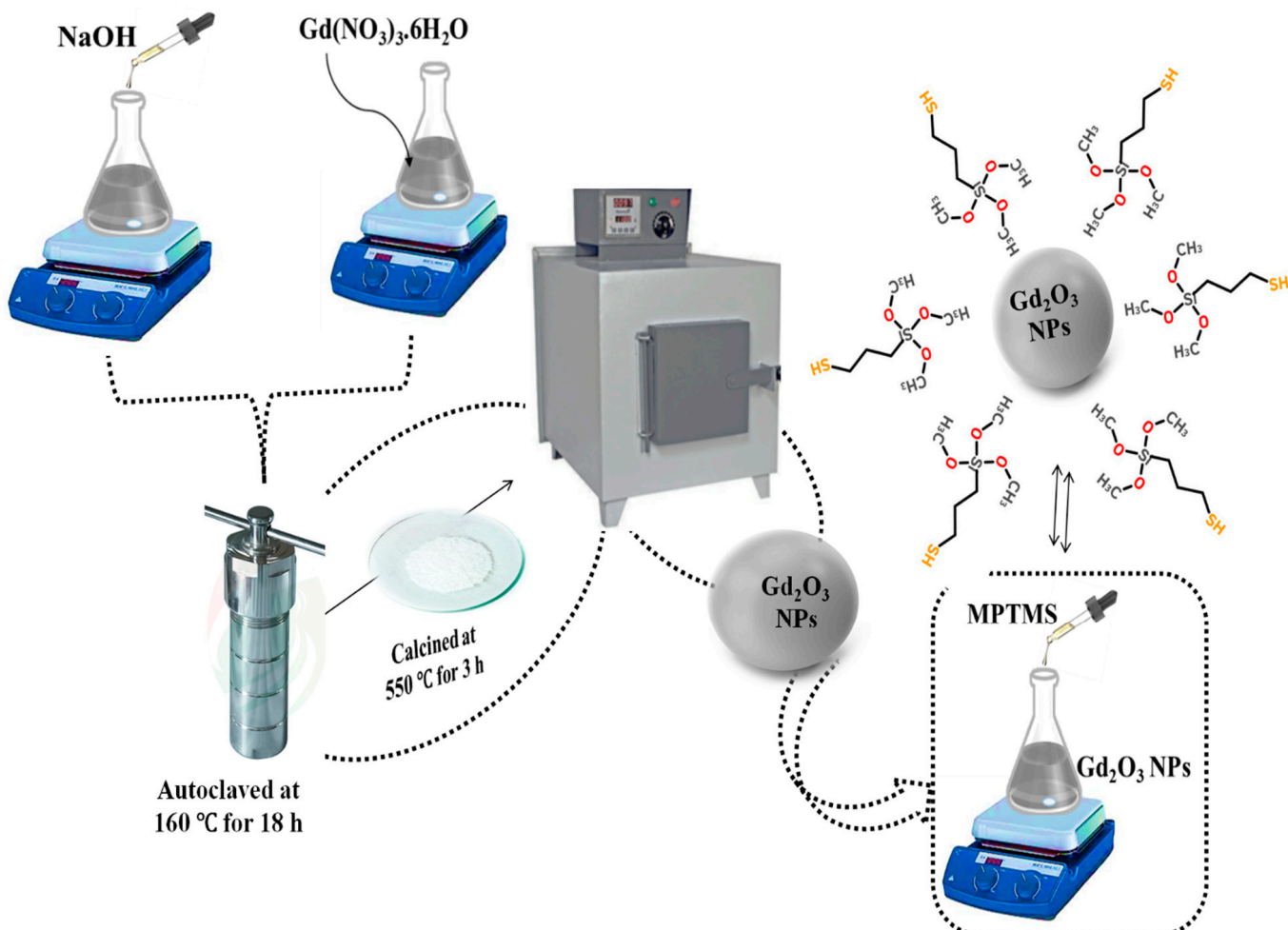
In this work, we proposed MPTMS functionalized Gd_2O_3 NPs synthesized from the hydrothermal method as a ratiometric fluorescent nanoprobe for Cys. The developed particles were systematically characterized to determine their size, shape, structure and chemical composition. The as formed MPTMS@ Gd_2O_3 nanoprobes have displayed excellent selectivity toward Cys, which significantly distinguished Cys from other amino acids. The fluorescence emission intensity of MPTMS@ Gd_2O_3 nanoprobes was linearly doused by increasing the concentration of Cys (turn “off”) in reaction media. The effective binding of surface modified MPTMS@ Gd_2O_3 with Cys could be responsible for the specific and efficient interaction with Cys, which further produced the quenching behavior in fluorescence intensity. These particles provide a contemporary approach for Cys sensing in complex environments with great accuracy.

2. Materials and Methods

2.1. Reagents and Synthetic Methodology to Prepare MPTMS@ Gd_2O_3 Nanoparticles

All HPLC-grade L-amino acids, including aspartic acid, glutamine, asparagine, tyrosine, histidine, leucine, isoleucine, arginine, alanine, methionine, glutamic acid, lysine, proline, phenylalanine, serine, tryptophan, threonine, glycine and valine, with 98% purity were bought from Sigma-Aldrich, Bengaluru, India. Gadolinium nitrate hexahydrate ($\text{Gd}(\text{NO}_3)_3 \cdot 6\text{H}_2\text{O}$, 99.9% pure), cysteine (Cys, ≥97% pure), GSH (98% pure) and (3-mercaptopropyl) trimethoxysilane (MPTMS, 95% pure) were also procured from Sigma-Aldrich. The concentrated HCl and NaOH pellets with 99% purity were obtained from Fisher Scientific of analytical grade. The size-controlled Gd_2O_3 NPs were fabricated via the hydrothermal method by the following procedure: Initially, the homogenous dispersion of 2 g of $\text{Gd}(\text{NO}_3)_3 \cdot 6\text{H}_2\text{O}$ was prepared in 20 mL distilled water under stirring conditions at 350 rpm. Afterwards, 1M NaOH solution was added in a drop-wise manner to a homogeneous solution of $\text{Gd}(\text{NO}_3)_3 \cdot 6\text{H}_2\text{O}$ and pH was adjusted to 10 and further stirred for 2 h at 350 rpm. Subsequently, the obtained solution was transferred into an 80 mL Teflon-lined

stainless steel autoclave (AICIL, Ambala, India). The hydrothermal treatment was given for 18 h at 160 °C (Scheme 1). After the completion of the reaction, the furnace was cooled down and the final mixture was filtered out to extract the sample. The obtained sample was further calcined at 550 °C for 3 h in a muffle furnace (AICIL, Ambala, India) to get Gd_2O_3 NPs. The particles collected were further washed thoroughly with ethanol and distilled water to remove the impurities.



Scheme 1. Schematic illustration showing the fabrication of MPTMS@ Gd_2O_3 NPs.

The exterior surface of Gd_2O_3 NPs was further modified to enhance their interaction with the analyte. For surface coating, 100 mg of Gd_2O_3 NPs were dispersed in 25 mL of ethanol under sonication at room temperature for 1 h. Thereafter, MPTMS solution (250 μL of 1wt%) was added in a dropwise manner under stirring conditions (Scheme 1). The resultant mixture was left under stirring conditions at 350 rpm for 36 h. The final mixture was filtered to obtain MPTMS@ Gd_2O_3 NPs. The collected powder was further washed with distilled water and ethanol and dried at 70 °C.

2.2. Instrumentation

Detailed information about the size and morphology of MPTMS@ Gd_2O_3 NPs was carried out by using transmission electron microscopy (TEM, Hitachi H-9500, Tokyo, Japan) and scanning electron microscopy (SEM, Hitachi SU8010, Hitachi, Tokyo, Japan). The optical behavior of synthesized particles was examined using a Jasco V-750 UV-visible Spectrophotometer (Jasco, Tokyo, Japan) in the range 200–650 nm. Further, the photoluminescence (PL) spectra were performed using the Edinburgh instrument FLS 980 (Bain Square, UK). A transparent quartz cuvette of 1.0 cm fixed path length was used during

the PL experiment. The Panalytical X’Pert Pro XRD powder diffractometer (Malvern, UK) using Cu K α radiation ($\lambda = 1.5406 \text{ \AA}$) with a scan rate of 2 degrees per minute with 2 θ range of 5–90° was used to examine the crystalline behavior of MPTMS@Gd₂O₃ nanoparticles. A Raman spectrophotometer (Wotton-under-Edge, UK) from Horiba, Lab RAM HR evolution was used to check the structural parameter for MPTMS@Gd₂O₃ nanoparticles. The hydrodynamic diameter of the particles was measured using a dynamic light scattering (DLS, Malvern (ZEN 1690), Worcestershire, UK) instrument. The Labman pH Multiparameter was used to check the pH of the reaction media. The functional properties of synthesized particles were studied using a Perkin Elmer 400 FTIR spectrometer (Waltham, MA, USA). The calcination was done on an AICIL furnace.

2.3. Detection Performance of MPTMS@Gd₂O₃

In a typical method, MPTMS@Gd₂O₃ NPs (1 mg) solution in 10 mL distilled water was treated with different concentrations of Cys ranging from 1–100 μm . The reaction mixture was sonicated for 2 min for complete homogenization. Afterwards, the fluorescence emission spectra for each prepared solution were monitored by exciting the sample at $\lambda_{\text{exc}} = 235 \text{ nm}$.

2.4. Interference and Selectivity Studies

The fluorescence emission spectra of MPTMS@Gd₂O₃ NPs were studied in the presence of various interfering compounds. Particularly, aspartic acid, glutamine, asparagine, tyrosine, histidine, leucine, isoleucine, arginine, alanine, methionine, glutamic acid, lysine, proline, phenylalanine, serine, tryptophan, threonine, glycine and valine were used to investigate the selectivity of developed nanoparticles. The solution of Cys (100 μm) was further mixed with an excess amount of other interfering amino acids (150 μm) in the presence of MPTMS@Gd₂O₃ NPs.

2.5. Recovery Studies of Cysteine (Cys)

The practical utilization of developed nanoparticles is highly important for enhancing the efficiency of developed sensors. For this analysis, recovery studies were carried out in the presence of serum samples. A dilute solution of Bovine serum albumin (BSA, 1 mg in 100 mL) was used during the experiment. The different amounts of Cys were spiked into the serum solution, i.e., 10 μm , 25 μm and 50 μm . Around 1.5 mL of the formed solution was further mixed with MPTMS@Gd₂O₃ NPs (1.5 mL) and fluorescence spectra were recorded for each sample.

3. Results and Discussion

3.1. Structural Characterization of MPTMS@Gd₂O₃ NPs

Figure 1 exhibits the typical XRD profile of MPTMS@Gd₂O₃ nanoparticles which exhibited well-defined diffraction peaks at 20.8°, 29.5°, 34.34°, 36.6°, 40.6°, 44.26°, 47.5°, 49.4°, 54.22° and 57.36° corresponding to (211), (222), (400), (411), (332), (134), (125), (440), (611) and (622) planes, respectively. The diffraction peaks well-resembled the cubic structure of Gd₂O₃ NPs and are in agreement with JCPDS data having No. 03-065-38131 [43]. The peak position was not influenced by surface functionalization with MPTMS. The outcomes suggested that the surface coating of MPTMS produced no variations in the nature and crystalline phase of the formed Gd₂O₃ NPs. The crystalline size of the formed particles estimated by employing the Scherer formula from more intense peaks came out to be 17 nm.

The morphologies of the prepared MPTMS@Gd₂O₃ nanoparticles (NPs) were examined by transmission electron microscopy (TEM) and scanning electron microscopy (SEM) (Figure 2). Figure 2a exhibits the typical TEM image of as-prepared MPTMS@Gd₂O₃ NPs which confirmed that the prepared material possesses almost spherical-shaped nanoparticles of various sizes.

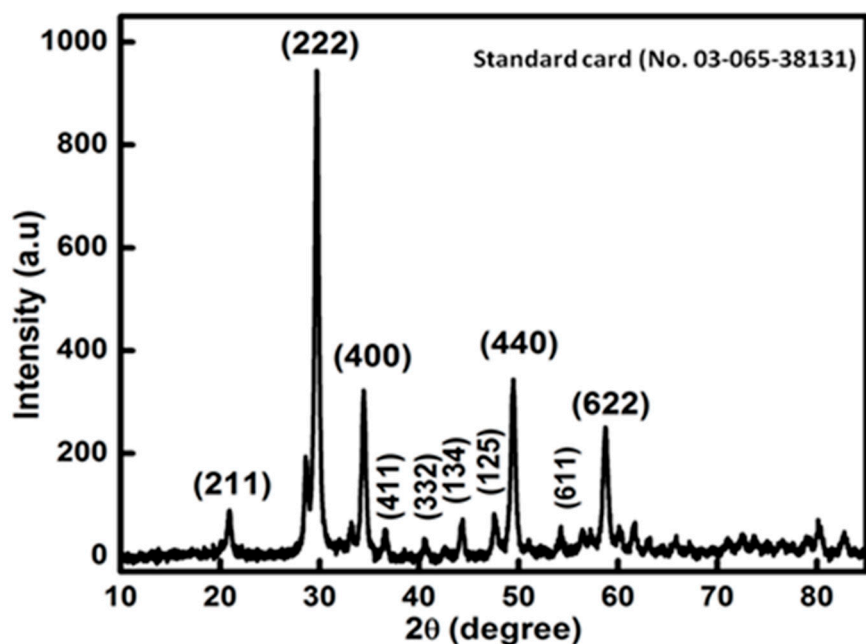


Figure 1. Typical XRD pattern of as-synthesized MPTMS@Gd₂O₃ nanoparticles.

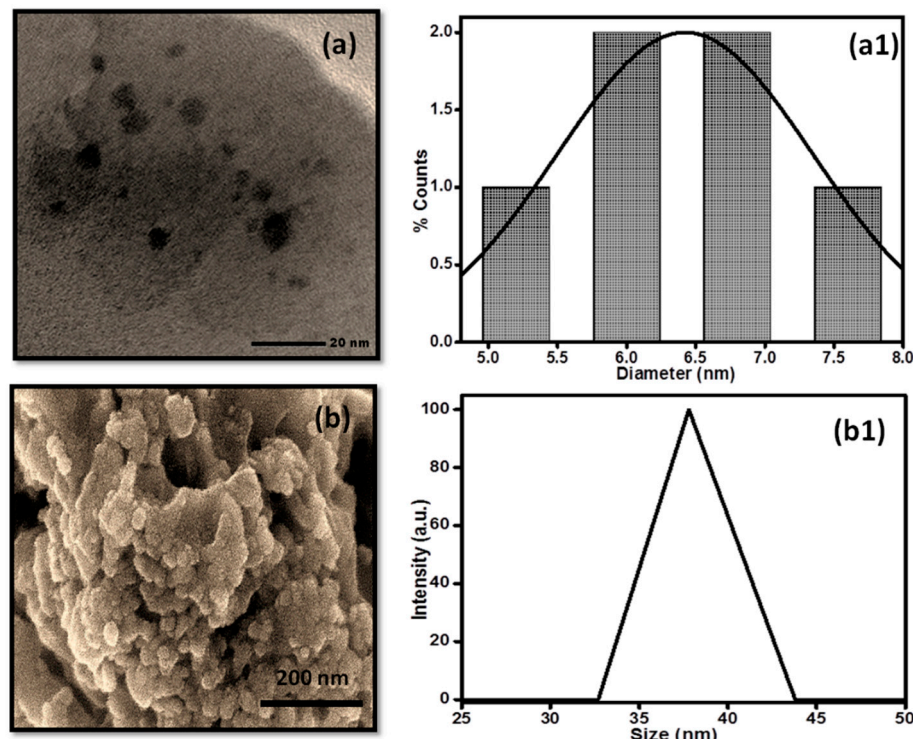


Figure 2. Typical (a) TEM image, (a1) Size distribution plot, (b) SEM image, and (b1) hydrodynamic diameter of MPTMS@Gd₂O₃ nanoparticles.

The corresponding size distribution plot for the synthesized MPTMS@Gd₂O₃ NPs revealed the typical 7 ± 1 nm mean average size for the prepared nanoparticles (Figure 2(a1)). The general morphologies of the synthesized MPTMS@Gd₂O₃ NPs were examined by SEM, which also confirmed the formation of spherical-shaped nanoparticles (Figure 2(b)). However, due to high-density growth, some agglomeration in the nanoparticles was also seen. Interestingly, the average hydrodynamic size of MPTMS@Gd₂O₃ NPs was found to be 35–45 nm through DLS analysis (Figure 2(b1)).

Raman and FTIR spectra were performed to examine the surface functional group and chemical composition of MPTMS@Gd₂O₃ NPs (Figure 3). Raman spectrum for formed particles was observed at an excitation of 785 nm laser in range 200–600 cm⁻¹. The strong Raman bands were located at 360, 395, 447 and 510 cm⁻¹ as shown in Figure 3a. The prominent peak at 360 cm⁻¹ was attributed to mixed modes of F_g + A_g, in cubic phase of Gd₂O₃ NPs. The peak obtained at 447 cm⁻¹ was found due to the independent F_g mode. Further, in the FTIR spectrum, the characteristic peak at 549.6 cm⁻¹ was attributed to the Gd-O stretching frequency (Figure 3b). The spectrum showing the peaks at 805.2 and 1038.7 cm⁻¹ is due to the Si-O-Si group in the MPTMS moiety. In addition, the peaks observed at 694.3 (C-O-Si) and 1262.4 cm⁻¹ (Si-O) confirmed the surface modification of Gd₂O₃ NPs using MPTMS molecules. The intense peak at 2927.9 cm⁻¹ represented the stretching frequency of the alkyl group in the MPTMS. However, the presence of bands at 1120 and 1436.9 cm⁻¹ symbolized the bending and asymmetric vibrations of the alkyl group (-CH₂-CH₂). The FTIR peak centered at 3434.29 cm⁻¹, which was mainly ascribed to the presence of OH stretching on the surface of MPTMS@Gd₂O₃ NPs. These outcomes clearly demonstrated the effective coating of MPTMS over the surface of Gd₂O₃ NPs.

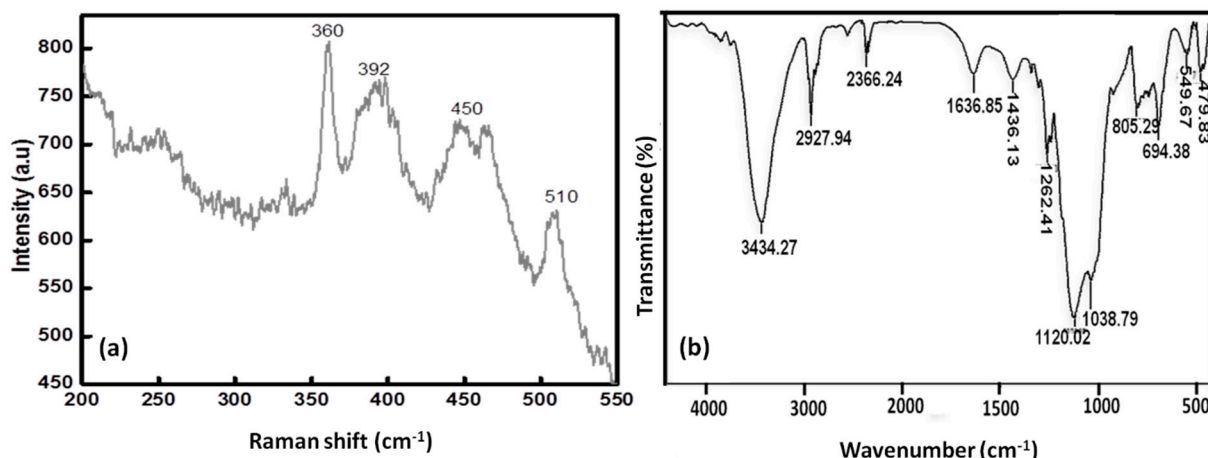


Figure 3. Typical (a) Raman scattering and (b) FTIR spectrum of as-synthesized MPTMS@Gd₂O₃ nanoparticles.

3.2. Optical Properties and Detection of Cys by MPTMS@Gd₂O₃ Nanoparticles

The optical properties of MPTMS@Gd₂O₃ NPs were assessed using UV-vis. and fluorescence spectroscopic analysis. The spectra displayed an absorption hump at 238 nm, with a broad peak at 272 nm (Figure 4a). This behavior was explained by the f-f transition (⁸S_{7/2} → ⁶I_J) of gadolinium (III) in MPTMS@Gd₂O₃ nanoparticles [20]. The band gap energies were also calculated by applying the Tauc creation and the value came out to be 5.84 eV (inset Figure 4a). Additionally, the UV-vis. spectra of Cys were also analyzed in the 200–800 nm range. The spectrum displayed a broad absorption band at 237 nm (Figure 4b). The corresponding band gap was found to be 5.59 eV (inset Figure 4b).

Further, the fluorescence spectra of MPTMS coated Gd₂O₃ NPs were checked at various excitations to analyze their emission profile. From the spectra, it was found that the emission spectra displayed maximum emission intensity at 650 nm with $\lambda_{exc} = 235$ nm (Figure 5a). Additionally, the water suspended MPTMS@Gd₂O₃ NPs showed good colloidal solubility as compared to Gd₂O₃ NPs. The emission behavior of MPTMS@Gd₂O₃ NPs was further investigated in the presence of various essential amino acids. The surface defect states of pristine Gd₂O₃ nanoparticles also supported the ability of MPTMS@Gd₂O₃ NPs towards cysteine sensing. The analysis was done for aspartic acid, glutamine, asparagine, tyrosine, histidine, leucine, isoleucine, Cys, arginine, alanine, methionine, glutamic acid, GSH, lysine, proline, phenylalanine, serine, tryptophan, threonine, glycine and valine (150 µm each). For the analysis, the properly sonicated sample of each suspension of amino acids with MPTMS@Gd₂O₃ NPs was employed for fluorescence studies. On interpreting

the results, it was found that the fluorescence intensity of MPTMS@Gd₂O₃ NPs was significantly affected in the presence of Cys (100 μm) (Figure 5b). The fluorescence band located at 650 nm was quenched by the addition of Cys. Further, the selectivity of the synthesized probe was investigated for aspartic acid, glutamine, asparagine, tyrosine, histidine, leucine, isoleucine, arginine, alanine, methionine, glutamic acid, lysine, proline, phenylalanine, serine, tryptophan, threonine, glycine and valine in the presence of Cys (Figure 5c). On interpreting the data, it was observed that the emission intensity of MPTMS@Gd₂O₃ NPs was nearly unaffected in the presence of Cys. These results suggested that the other amino acids except Cys did not influence the emission intensity of MPTMS@Gd₂O₃ NPs in the presence of Cys in the aqueous samples. The outcomes supported the selectivity and specificity of the developed MPTMS based Gd₂O₃ sensor toward the detection of Cys. The probable reason behind the sensing of Cys is mainly explained by the effective collision between the fluorophoric group of MPTMS@Gd₂O₃ NPs and the quencher (cysteine). These collisions had the propensity to produce a non-fluorescent ground state complex via the transference of energy and molecular rearrangements. This complexation was promoted the accumulation of molecules and augmented the intra-molecular charge transfer (ICT) between the surface functional group of Gd₂O₃ and cysteine.

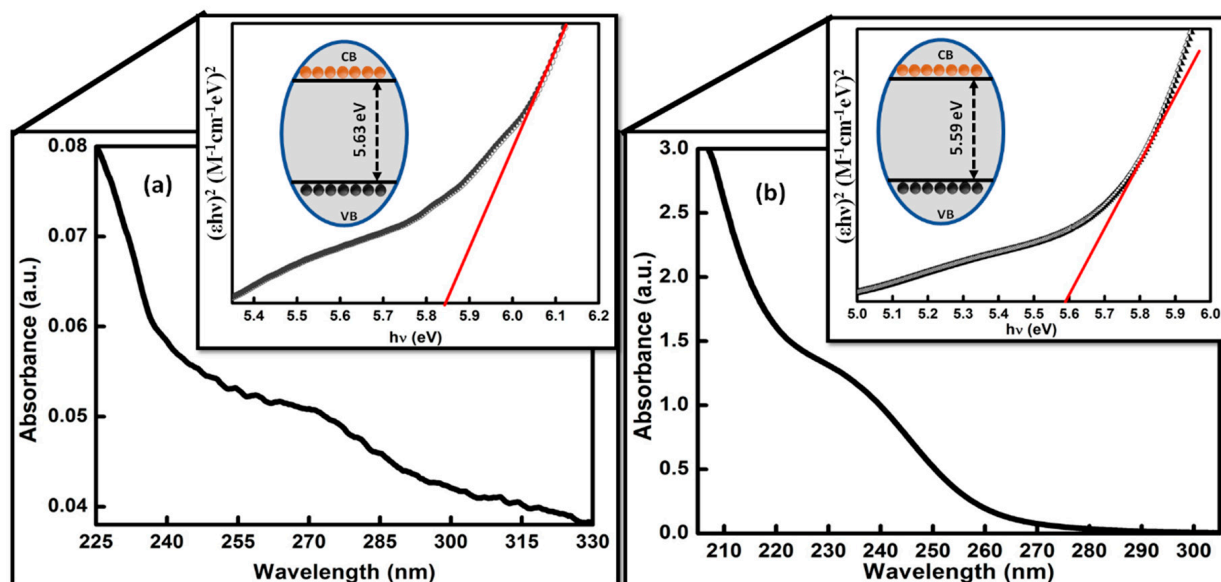


Figure 4. (a,b) UV-vis. spectra and (inset (a,b)) showing the band gap of MPTMS@Gd₂O₃ NPs and Cys, respectively.

3.3. Mechanistic Aspects of Cys Sensing by MPTMS@Gd₂O₃ NPs

Generally, the fluorescence quenching of any kind of developed sensor and the corresponding analyte has been explained by using the Inner filter effect (IFE), intermolecular charge transfer, Förster resonant energy transfer (FRET), photo-induced electron transfer (PET), and static and dynamic quenching effect on the basis of the obtained results [44–46]. In the current work, the presence of an analyte, i.e., Cys produced an appreciable range of quenching of around 80.4% as compared to MPTMS@Gd₂O₃ NPs. To chalk out the mechanistic reasoning behind the quenching, the absorption profile and band gap of MPTMS@Gd₂O₃ nanoparticles and Cys were investigated carefully (Figure 4). The results showed a small difference of around 0.04 eV between the band gap energies of MPTMS@Gd₂O₃ NPs and Cys. This small variation in the band gap enhanced the possibility of the photo-induced electron transfer (PET) phenomenon among MPTMS@Gd₂O₃ NPs and Cys. To explain further, it was quite possible that the electrons from the conduction band of MPTMS@Gd₂O₃ NPs was easily transferred from the highest occupied molecular orbital (HOMO) to the lowest unoccupied molecular orbital (LUMO) (Figure 6a).

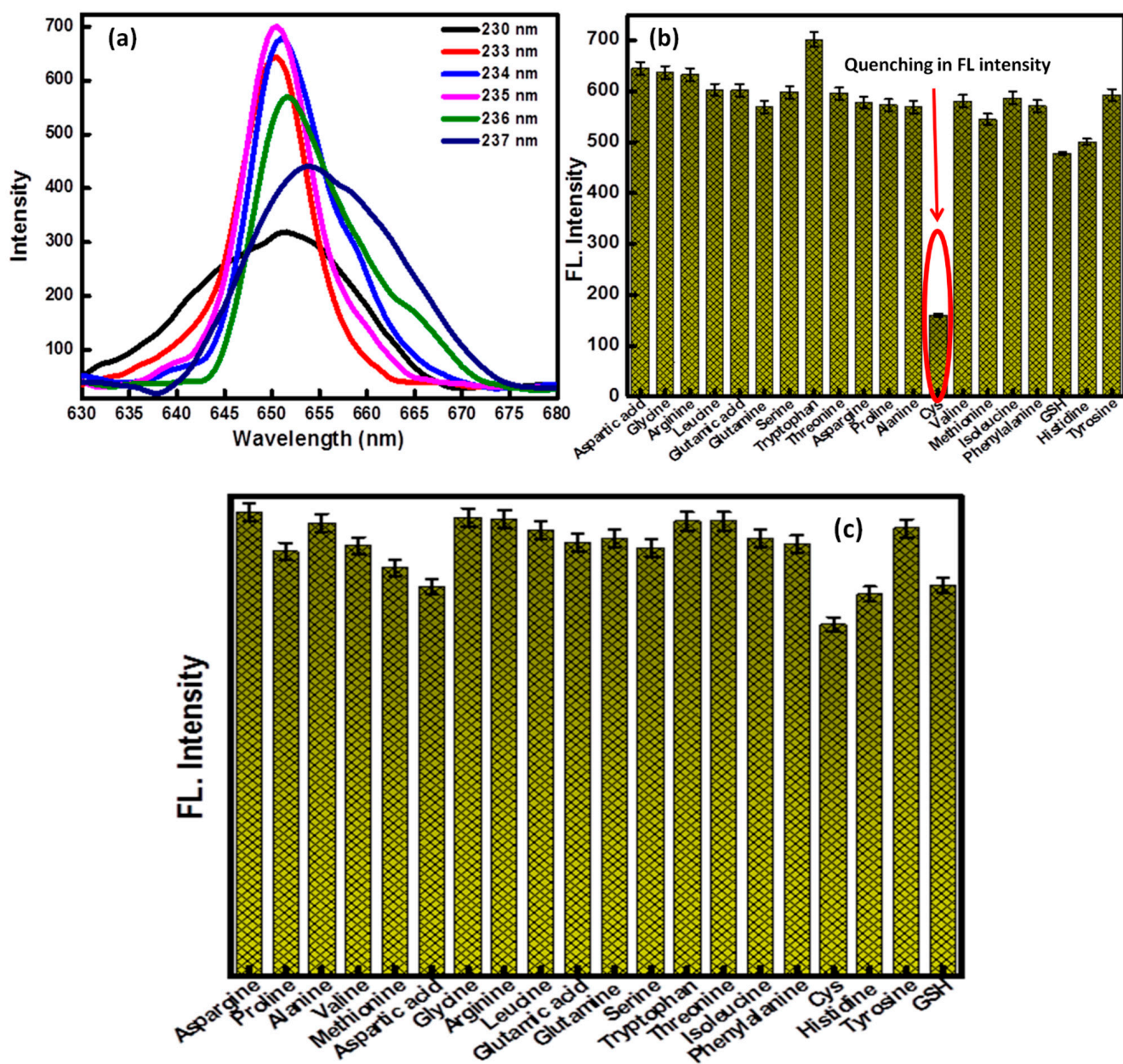


Figure 5. (a) The optimization of fluorescence emission intensity of MPTMS@Gd₂O₃ NPs at various excitation wavelengths. The corresponding changes in the fluorescence intensity of MPTMS@Gd₂O₃ NPs (b) in the presence of various amino acids and (c) their selectivity results.

Then, this excited electron is transferred in the form of energy to the LUMO of Cys. These outcomes suggested that quenching in the fluorescence emission intensity of MPTMS@Gd₂O₃ NPs is mainly explained via the PET mechanism in the presence of Cys. However, the possibility of the IFE and FRET mechanism was ruled out due to the non-overlapping absorption peak of Cys with the emission spectra of MPTMS@Gd₂O₃ NPs. However, the possibility of energy transfers between the sensor and analyte through direct energy transfer or the Dexter mechanism was also studied in detail [47]. In this phenomenon, energy transfer between adjacent molecules takes place. In the Dexter energy transfer process, there is a possibility of energy transfer from the LUMO of MPTMS@Gd₂O₃ NPs to the LUMO of Cys, and simultaneously an electron from the ground state of Cys was transferred to the ground state of MPTMS@Gd₂O₃ NPs (Figure 6b). Thus, the energy transfer in the case of the Dexter mechanism is related to two electron transfer processes.

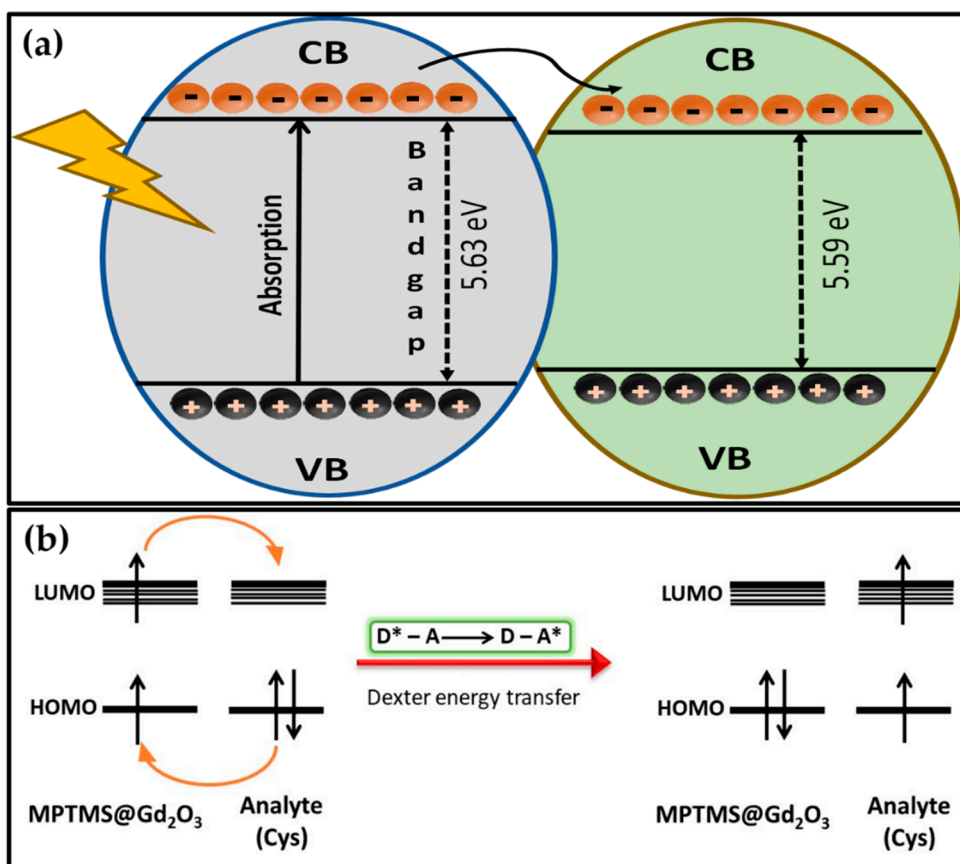


Figure 6. (a) The proposed mechanism of Cys quenching through PET energy transfer and (b) Dexter energy transfer between MPTMS@Gd₂O₃ nanoparticles and Cys molecules.

In the current system, both MPTMS@Gd₂O₃ and Cys displayed the absorption hump in the same region. Therefore, there is a possibility of ground state complex formation between the chosen probe and analyte before excitation. The coating template of Gd₂O₃ NPs, i.e., MPTMS is highly interactive due to the presence of free binding sites. Thus, the -SH group of MPTMS has the probability of interacting with any of the -COOH and -NH₂ group present in the Cys molecule. Such interaction has the tendency to promote the quenching behavior of MPTMS@Gd₂O₃ by Cys. However, this probability is neglected, as such interaction is possible to exist in other amino acids due to the existence of the same substituent. If this interaction is a responsible factor, then other amino acids should also have the tendency to influence the emission behavior of MPTMS@Gd₂O₃ NPs. Therefore, the mechanistic aspect of MPTMS@Gd₂O₃ NPs with Cys is only validated by energy transfer in this current work.

Along with PET, there is a high probability of effective collision between the fluorophoric group of MPTMS@Gd₂O₃ NPs and quencher (cysteine). These collisions had the propensity to produce a non-fluorescent ground state complex via the transference of energy and molecular rearrangements. This complexation produced the accumulation of molecules and augmented the intra-molecular charge transfer (ICT) between the surface functional group of Gd₂O₃ and cysteine.

The respective effect of the pH of reaction media ranging from 2 to 12 on the emission intensity of MPTMS@Gd₂O₃ was performed to explore the scope of prepared nanoparticles (Figure 7a). On interpreting the data, it was found that the fluorescence intensity of MPTMS@Gd₂O₃ was found to be less at pH 5 and at pH = 10. However, the fluorescence intensity of MPTMS@Gd₂O₃ was found to be maximum at pH = 7. Further, the fluorescence emission behavior of MPTMS@Gd₂O₃ was studied as a function of different concentrations of Cys (0–100 μm) in the reaction media (Figure 7b). From the data, it was found that the

addition of Cys into MPTMS@Gd₂O₃ solution caused apparent changes in the fluorescence response. The emission intensity showed linear decrement by increasing the concentration of Cys in the system (Figure 7c). The detection limit for Cys was calculated by $3S/\sigma$ and obtained to be 42 nm. The results supported the excellent sensitivity of the developed sensor toward the detection of Cys. Therefore, the developed fluorescence-based sensor provided an alternative and effective approach toward the detection of Cys in biological fluids, urine and water. The present method also exhibited a competitive sensing range and low detection limit compared to other methods. The outcomes of the work were compared in terms of linear sensitive range and detection limit with other reported methods (Table 1).

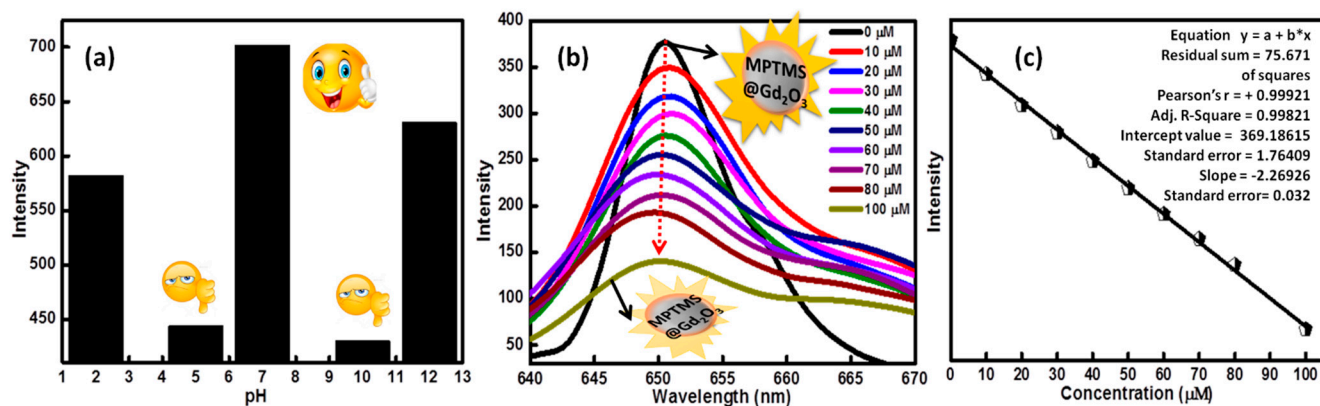


Figure 7. The change in the fluorescence response of MPTMS@Gd₂O₃ NPs as a function of (a) pH and (b) increasing concentration of Cys and (c) along with the corresponding linear plot between fluorescence intensity of developed nanoparticles in the presence of different concentrations of Cys.

Table 1. Comparison of the linear range and detection limit of the proposed sensor with other reported methods for the detection of Cys.

Material	Linear Concentration (μM)	Detection Limit (μM)	References
DNA-Ag NCs	0–5	0.134	[48]
PEI-Ag NCs	0.1–10	0.042	[49]
N,S-CQDs-Cu ²⁺	10–200	0.540	[50]
Benzothiazole-based probe	0–100	0.800	[51]
CdTe-Hg ²⁺	2–20	0.600	[52]
Fluorescein-based probe	0.2–1	0.600	[53]
Hg ²⁺ +Citrate-Au NPs	0.035–1.53	9	[54]
NC-dots/Au NPs	0.02–2	8	[19]
GSH-Ag NCs	2–3000	0.51	[1]
Surface modified CdS	0.5–10	0.5	[16]
Present work	0–100	0.042	

3.4. Recovery Studies

The potential scope of the prepared sensor was further tested in the presence of serum samples. The feasibility of the method for the quantification of Cys was determined in different spiked serum samples. The preparation of the samples was done using the standard addition method [55–60]. The spiking was performed with three different concentrations, i.e., 10, 25 and 50 μM concentrations of Cys in the serum solution. The emission spectra were recorded for each spiked amount of Cys [61–65]. All the prepared samples showed a recovery of around 95 to 101% of Cys in the presence of serum samples (Table 2). These

outcomes supported the high sensitivity and recovery rate of MPTMS@Gd₂O₃ towards the direct determination of Cys in biological fluids.

Table 2. Percentage recovery of Cys into spiked samples by using MPTMS@Gd₂O₃ NPs.

S. No.	Spiked (μm)	Found (μm)	Recovery (%)
1.	10	9.55	95.5
2.	25	25.20	100.8
3.	50	49.1	98.2

4. Conclusions

The current work summarized the fabrication of MPTMS@Gd₂O₃ NPs by using the hydrothermal method. The surface functionalization of Gd₂O₃ NPs with MPTMS offered better control over the solubility and size of Gd₂O₃ NPs and further enhanced its fluorescence sensing aptitude toward Cys by offering a “fluorescence turn-off” sensor in aqueous media. The as-prepared MPTMS@Gd₂O₃ NPs showed an emission peak at 650 nm. However, the fluorescence intensity displayed a significant quenching of around 80.4% with Cys amino acids. The developed MPTMS@Gd₂O₃ NPs -based fluorescence strategy was successfully used for assaying Cys in the presence of various interfering amino acids with a remarkable range of LODs of around 42 nm. Additionally, the developed sensor was successfully applied for the analysis of Cys in the presence of serum samples with high sensitivity and precision values. All of the prepared samples showed a recovery of around 95 to 101% of Cys in the presence of serum samples. The developed sensor possesses the high scope to act as a miniaturized analytical tool using a simple fluorescence-based method for the sensing of Cys.

Author Contributions: S.K.; collected the literature, performed all the experiments, formal analysis, methodologies, software and write the manuscript, G.R.C.; Read, correct and revise the manuscript, S.C. and A.U.; Project administration, data validation, curation, conceptualization and writing (original draft). All authors have read and agreed to the published version of the manuscript.

Funding: Savita Chaudhary is thankful for the DST Inspire Faculty award [IFACH-17], Haryana State Council for Science and Technology [HSCSIT/R&D/2020/476], DST Chandigarh [S&T&RE/RP/147/e-2873/(19-20)/Sanc/12/2019/1878-1885], and [S&T&RE/RP/147/e-2873/(22-23)/Sanc/09/2022/907-915], and DST Purse grants II for financial assistance. Ganga Ram is thankful to DST, SERB/F/8171/2015-16 and UGC (F. No. 194-2/2016 IC) for providing financial support. Sushil Kumar is thankful to UGC for JRF and SRF fellowship (Ref No: 20/12/2015(ii) EU-V).

Institutional Review Board Statement: Not applicable.

Informed Consent Statement: Not applicable.

Data Availability Statement: All data that support the findings of this study are included within the article.

Acknowledgments: Authors are thankful to CIL, Panjab University for providing instrumental facilities. Ahmad Umar would like to acknowledge Najran University, Saudi Arabia for the support.

Conflicts of Interest: The authors declare no conflict of interest.

References

- Cao, N.; Zhou, H.; Tan, H.; Qi, R.; Chen, J.; Zhang, S.; Xu, J. Turn-on fluorescence detection of cysteine with glutathione protected silver nanoclusters. *Methods Appl. Fluoresc.* **2019**, *7*, 034004. [[CrossRef](#)] [[PubMed](#)]
- Zhou, Y.; Zhou, T.; Zhang, M.; Shi, G. A DNA-scaffolded silver nanocluster/Cu²⁺ ensemble as a turn-on fluorescent probe for histidine. *Analyst* **2014**, *139*, 3122–3126. [[CrossRef](#)] [[PubMed](#)]
- Xiong, P.; Zhang, Y.; Zhang, J.; Baek, S.H.; Zeng, L.; Yao, Y.; Park, H.S. Recent progress of artificial interfacial layers in aqueous Zn metal batteries. *EnergyChem* **2022**, *4*, 100076. [[CrossRef](#)]
- Xie, H.; Xu, S.; Sang, L.; Du, S.; Zhu, F. Detection of Key Proteins in Obstetric Preeclampsia by Nanocomposites Using Gold Nanoparticles/DNA/Methylene Blue. *Sci. Adv. Mater.* **2021**, *13*, 321–330. [[CrossRef](#)]

5. Cui, M.-L.; Liu, J.-M.; Wang, X.-X.; Lin, L.-P.; Jiao, L.; Zhang, L.-H.; Zheng, Z.-Y.; Lin, S.-Q. Selective determination of cysteine using BSA-stabilized gold nanoclusters with red emission. *Analyst* **2012**, *137*, 5346–5351. [[CrossRef](#)] [[PubMed](#)]
6. Khan, Z.G.; Patil, P.O. Design and synthesis of poly-L-lysine-functionalized graphene quantum dots sensor for specific detection of cysteine and homocysteine. *Mater. Chem. Phys.* **2022**, *276*, 125383. [[CrossRef](#)]
7. Shariati, S.; Khayatian, G. The colorimetric and microfluidic paper-based detection of cysteine and homocysteine using 1,5-diphenylcarbazide-capped silver nanoparticles. *RSC Adv.* **2021**, *11*, 3295–3303. [[CrossRef](#)] [[PubMed](#)]
8. Peixoto, E.; Atorrasagasti, C.; Aquino, J.B.; Militello, R.; Bayo, J.; Fiore, E.; Piccioni, F.; Salvatierra, E.; Alaniz, L.; García, M.G.; et al. SPARC (secreted protein acidic and rich in cysteine) knockdown protects mice from acute liver injury by reducing vascular endothelial cell damage. *Gene Ther.* **2015**, *22*, 9–19. [[CrossRef](#)]
9. Yang, X.; Guo, Y.; Strongin, R.M. Conjugate Addition/Cyclization Sequence Enables Selective and Simultaneous Fluorescence Detection of Cysteine and Homocysteine. *Angew. Chem.* **2011**, *123*, 10878–10881. [[CrossRef](#)]
10. Yalikun, N.; Xu, L.; Yang, X.Q.; Wang, Q. Highly Sensitive Electrochemical Sensor for the Detection of Hydroquinone and Catechol Based on Biomass Derived Activated Carbon. *Sci. Adv. Mater.* **2021**, *13*, 2178–2184. [[CrossRef](#)]
11. Nekrassova, O. Analytical determination of homocysteine: A review. *Talanta* **2003**, *60*, 1085–1095. [[CrossRef](#)]
12. Zhang, W.; Li, P.; Geng, Q.; Duan, Y.; Guo, M.; Cao, Y. Simultaneous Determination of Glutathione, Cysteine, Homocysteine, and Cysteinylglycine in Biological Fluids by Ion-Pairing High-Performance Liquid Chromatography Coupled with Precolumn Derivatization. *J. Agric. Food Chem.* **2014**, *62*, 5845–5852. [[CrossRef](#)] [[PubMed](#)]
13. Manibalan, G.; Murugadoss, G.; Marimuthu, R.; Rajabathar, J.R.; Kumar, M.R. Facile synthesis of heterostructure NiO–SnO₂ nanocomposite for selective electrochemical determination of l-cysteine. *J. Mater. Sci. Mater. Electron.* **2022**, *33*, 6592–6602. [[CrossRef](#)]
14. Kumar, S.; Chaudhary, G.R.; Umar, A.; Chaudhary, S. High-performance enzyme-free detection of L-Cysteine using (3-mercaptopropyl) trimethoxysilane functionalized Gd₂O₃ nanoparticles. *J. Alloy. Compounds.* **2022**, *905*, 164059. [[CrossRef](#)]
15. Chen, S.; Chi, M.; Zhu, Y.; Gao, M.; Wang, C.; Lu, X. A Facile synthesis of superparamagnetic Fe₃O₄ nanofibers with superior peroxidase-like catalytic activity for sensitive colorimetric detection of l-cysteine. *Appl. Surf. Sci.* **2018**, *440*, 237–244. [[CrossRef](#)]
16. Negi, D.P.S.; Chanu, T.I. Surface-modified CdS nanoparticles as a fluorescent probe for the selective detection of cysteine. *Nanotechnology* **2008**, *19*, 465503. [[CrossRef](#)]
17. Ning, Z.; Wu, S.; Liu, G.; Ji, Y.; Jia, L.; Niu, X.; Ma, R.; Zhang, Y.; Xing, G.-W. Water-soluble AIE-Active Fluorescent Organic Nanoparticles: Design, Preparation and Application for Specific Detection of Cysteine over Homocysteine and Glutathione in Living Cells. *Chem. Asian J.* **2019**, *14*, 2220–2224. [[CrossRef](#)]
18. Raj, D.R.; Sudarsanakumar, C. Surface plasmon resonance based fiber optic sensor for the detection of cysteine using diosmin capped silver nanoparticles. *Sens. Actuators A Phys.* **2017**, *253*, 41–48. [[CrossRef](#)]
19. Deng, J.; Lu, Q.; Hou, Y.; Liu, M.; Li, H.; Zhang, Y.; Yao, S. Nanosensor Composed of Nitrogen-Doped Carbon Dots and Gold Nanoparticles for Highly Selective Detection of Cysteine with Multiple Signals. *Anal. Chem.* **2015**, *87*, 2195–2203. [[CrossRef](#)]
20. Ansari, A.A.; Ahmad, N.; Labis, J.P. Highly colloidal luminescent porous Tb-doped gadolinium oxide nanoparticles: Photophysical and luminescent properties. *J. Photochem. Photobiol. A Chem.* **2019**, *371*, 10–16. [[CrossRef](#)]
21. Zhang, Z.; Wang, L.; Li, G.; Ye, B. Lanthanide coordination polymer nanoparticles as a turn-on fluorescence sensing platform for simultaneous detection of histidine and cysteine. *Analyst* **2017**, *142*, 1821–1826. [[CrossRef](#)] [[PubMed](#)]
22. Li, W.; Guo, X.; Geng, P.; Du, M.; Jing, Q.; Chen, X.; Zhang, G.; Li, H.; Xu, Q.; Braunstein, P.; et al. Rational Design and General Synthesis of Multimetallic Metal–Organic Framework Nano-Octahedra for Enhanced Li–S Battery. *Adv. Mater.* **2021**, *33*, 2105163. [[CrossRef](#)] [[PubMed](#)]
23. Chauhan, P.; Chaudhary, S. Role of surface modification on selenium nanoparticles: Enumerating the optical, thermal and structural properties. *Opt. Mater.* **2019**, *97*, 109380. [[CrossRef](#)]
24. Xue, S.-F.; Lu, L.-F.; Wang, Q.-X.; Zhang, S.; Zhang, M.; Shi, G. An integrated logic system for time-resolved fluorescent “turn-on” detection of cysteine and histidine base on terbium (III) coordination polymer–copper (II) ensemble. *Talanta* **2016**, *158*, 208–213. [[CrossRef](#)] [[PubMed](#)]
25. Kumar, S.; Mehta, D.; Chaudhary, S.; Chaudhary, G.R. Pr@Gd₂O₃ nanoparticles: An effective fluorescence sensor for herbicide 2,4-dichlorophenoxyacetic acid. *J. Mol. Liq.* **2021**, *324*, 114712. [[CrossRef](#)]
26. Chen, Z.; Jia, H.; Zhang, X.; Liu, J.; Zeng, S.; Li, Y.; Ma, Z.; Dong, G.; Qiu, J. BaCl₂: Er³⁺—A High Efficient Upconversion Phosphor for Broadband Near-Infrared Photoresponsive Devices. *J. Am. Ceram. Soc.* **2015**, *98*, 2508–2513. [[CrossRef](#)]
27. Chen, X.; Xu, W.; Song, H.; Chen, C.; Xia, H.; Zhu, Y.; Zhou, D.; Cui, S.; Dai, Q.; Zhang, J. Highly Efficient LiYF₄: Yb³⁺, Er³⁺ Upconversion Single Crystal under Solar Cell Spectrum Excitation and Photovoltaic Application. *ACS Appl. Mater. Interfaces* **2016**, *8*, 9071–9079. [[CrossRef](#)]
28. Bagheri, A.; Arandiyan, H.; Boyer, C.; Lim, M. Lanthanide-Doped Upconversion Nanoparticles: Emerging Intelligent Light-Activated Drug Delivery Systems. *Adv. Sci.* **2016**, *3*, 1500437. [[CrossRef](#)]
29. Guo, K.; Li, M.; Fang, X.; Luoshan, M.; Bai, L.; Zhao, X. Performance enhancement in dye-sensitized solar cells by utilization of a bifunctional layer consisting of core–shell β-NaYF₄:Er³⁺/Yb³⁺@SiO₂ submicron hexagonal prisms. *J. Power Sources* **2014**, *249*, 72–78. [[CrossRef](#)]
30. Feng, L.; He, F.; Liu, B.; Yang, G.; Gai, S.; Yang, P.; Li, C.; Dai, Y.; Lv, R.; Lin, J. g-C₃N₄ Coated Upconversion Nanoparticles for 808 nm Near-Infrared Light Triggered Phototherapy and Multiple Imaging. *Chem. Mater.* **2016**, *28*, 7935–7946. [[CrossRef](#)]

31. Chaudhary, S.; Kumari, M.; Chauhan, P.; Chaudhary, G.R. Upcycling of plastic waste into fluorescent carbon dots: An environmentally viable transformation to biocompatible C-dots with potential prospective in analytical applications. *Waste Manag.* **2021**, *120*, 675–686. [[CrossRef](#)] [[PubMed](#)]
32. Chen, C.-W.; Chan, Y.-C.; Hsiao, M.; Liu, R.-S. Plasmon-Enhanced Photodynamic Cancer Therapy by Upconversion Nanoparticles Conjugated with Au Nanorods. *ACS Appl. Mater. Interfaces* **2016**, *8*, 32108–32119. [[CrossRef](#)] [[PubMed](#)]
33. Dutta, S.; Patra, A.K.; De, S.; Bhaumik, A.; Saha, B. Self-Assembled TiO₂ Nanospheres by Using a Biopolymer as a Template and Its Optoelectronic Application. *ACS Appl. Mater. Interfaces* **2012**, *4*, 1560–1564. [[CrossRef](#)] [[PubMed](#)]
34. Xu, J.; Yang, P.; Sun, M.; Bi, H.; Liu, B.; Yang, D.; Gai, S.; He, F.; Lin, J. Highly Emissive Dye-Sensitized Upconversion Nanostructure for Dual-Photosensitizer Photodynamic Therapy and Bioimaging. *ACS Nano* **2017**, *11*, 4133–4144. [[CrossRef](#)] [[PubMed](#)]
35. Fang, J.; Chandrasekharan, P.; Liu, X.-L.; Yang, Y.; Lv, Y.-B.; Yang, C.-T.; Ding, J. Manipulating the surface coating of ultra-small Gd₂O₃ nanoparticles for improved T1-weighted MR imaging. *Biomaterials* **2014**, *35*, 1636–1642. [[CrossRef](#)]
36. Huang, C.-C.; Su, C.-H.; Li, W.-M.; Liu, T.-Y.; Chen, J.-H.; Yeh, C.-S. Bifunctional Gd₂O₃/C Nanoshells for MR Imaging and NIR Therapeutic Applications. *Adv. Funct. Mater.* **2009**, *19*, 249–258. [[CrossRef](#)]
37. Li, I.-F.; Su, C.-H.; Sheu, H.-S.; Chiu, H.-C.; Lo, Y.-W.; Lin, W.-T.; Chen, J.-H.; Yeh, C.-S. Gd₂O(CO₃)₂ · H₂O Particles and the Corresponding Gd₂O₃: Synthesis and Applications of Magnetic Resonance Contrast Agents and Template Particles for Hollow Spheres and Hybrid Composites. *Adv. Funct. Mater.* **2008**, *18*, 766–776. [[CrossRef](#)]
38. Ahmad, M.W.; Xu, W.; Kim, S.J.; Baeck, J.S.; Chang, Y.; Bae, J.E.; Chae, K.S.; Park, J.A.; Kim, T.J.; Lee, G.H. Potential dual imaging nanoparticle: Gd₂O₃ nanoparticle. *Sci. Rep.* **2015**, *5*, 8549. [[CrossRef](#)] [[PubMed](#)]
39. Zhou, C.; Wu, H.; Huang, C.; Wang, M.; Jia, N. Facile Synthesis of Single-Phase Mesoporous Gd₂O₃: Eu Nanorods and Their Application for Drug Delivery and Multimodal Imaging. *Part. Part. Syst. Charact.* **2014**, *31*, 675–684. [[CrossRef](#)]
40. Lee, H.J.; Park, J.; Choi, S.; Son, J.; Oh, M. Synthesis and photoluminescence properties of Eu³⁺@doped silica@coordination polymer core–shell structures and their calcinated silica@Gd₂O₃: Eu and hollow Gd₂O₃: Eu microsphere products. *Small* **2013**, *9*, 561–569. [[CrossRef](#)]
41. Kryza, D.; Taleb, J.; Janier, M.; Marmuse, L.; Miladi, I.; Bonazza, P.; Louis, C.; Perriat, P.; Roux, S.; Tillement, O.; et al. Biodistribution Study of Nanometric Hybrid Gadolinium Oxide Particles as a Multimodal SPECT/MR/Optical Imaging and Theragnostic Agent. *Bioconjug. Chem.* **2011**, *22*, 1145–1152. [[CrossRef](#)] [[PubMed](#)]
42. Chaudhary, S.; Kumar, S.; Mehta, S.; Umar, A. Ethylene Glycol Functionalized Gadolinium Oxide Nanoparticles as a Potential Electrochemical Sensing Platform for Hydrazine and p-Nitrophenol. *Coatings* **2019**, *9*, 633. [[CrossRef](#)]
43. Jain, A.; A Hirata, G.; Fariñas, M.H.; Castillón, F.F. Synthesis and characterization of (3-Aminopropyl) trimethoxy-silane (APTMS) functionalized Gd₂O₃: Eu³⁺ red phosphor with enhanced quantum yield. *Nanotechnology* **2015**, *27*, 065601. [[CrossRef](#)]
44. Malik, A.H.; Iyer, P.K. Conjugated Polyelectrolyte Based Sensitive Detection and Removal of Antibiotics Tetracycline from Water. *ACS Appl. Mater. Interfaces* **2017**, *9*, 4433–4439. [[CrossRef](#)] [[PubMed](#)]
45. Chen, S.; Yu, Y.-L.; Wang, J.-H. Inner filter effect-based fluorescent sensing systems: A review. *Anal. Chim. Acta* **2018**, *999*, 13–26. [[CrossRef](#)] [[PubMed](#)]
46. Halawa, M.I.; Wu, F.; Fereja, T.H.; Lou, B.; Xu, G. One-pot green synthesis of supramolecular β-cyclodextrin functionalized gold nanoclusters and their application for highly selective and sensitive fluorescent detection of dopamine. *Sens. Actuators B Chem.* **2018**, *254*, 1017–1024. [[CrossRef](#)]
47. Filatov, M.A. Heavy-atom-free BODIPY photosensitzers with intersystem crossing mediated by intramolecular photoinduced electron transfer. *Org. Biomol. Chem.* **2020**, *18*, 10–27. [[CrossRef](#)]
48. Li, C.; Wei, C. DNA-functionlized silver nanoclusters as label-free fluorescent probe for the highly sensitive detection of biothiols and acetylcholinesterase activity. *Sens. Actuators B Chem.* **2017**, *240*, 451–458. [[CrossRef](#)]
49. Zhang, N.; Qu, F.; Luo, H.Q.; Li, N.B. Sensitive and selective detection of biothiols based on target-induced agglomeration of silvernanoclusters. *Biosens. Bioelectron.* **2013**, *42*, 214–218. [[CrossRef](#)]
50. Wu, H.; Jiang, J.; Gu, X.; Tong, C. Nitrogen and sulfur co-doped carbon quantum dots for highly selective and sensitive fluorescent detection of Fe(III) ions and L-cysteine. *Mikrochim. Acta* **2017**, *184*, 2291–2298. [[CrossRef](#)]
51. Zhang, H.; Feng, W.; Feng, G. A simple and readily available fluorescent turn-on probe for cysteine detection and bioimaging in living cells. *Dye. Pigment.* **2017**, *139*, 73–78. [[CrossRef](#)]
52. Han, B.; Yuan, J.; Wang, E. Sensitive and Selective Sensor for Biothiols in the Cell Based on the Recovered Fluorescence of the CdTe Quantum Dots–Hg(II) System. *Anal. Chem.* **2009**, *81*, 5569–5573. [[CrossRef](#)] [[PubMed](#)]
53. Liu, Y.; Xiang, K.; Tian, B.; Zhang, J. Rhodol-based far-red fluorescent probe for the detection of cysteine and homocysteine over glutathione. *Luminescence* **2017**, *32*, 78–85. [[CrossRef](#)]
54. Xu, H.; Wang, Y.; Huang, X.; Li, Y.; Zhang, H.; Zhong, X. Hg²⁺-mediated aggregation of gold nanoparticles for colorimetric screening of biothiols. *Analyst* **2012**, *137*, 924–931. [[CrossRef](#)] [[PubMed](#)]
55. Tan, G.; Li, B.; Zhang, Y.; Zhang, R.; Wang, L.; Liu, F.; Shan, F. Targeted Fluorescence Imaging and Anti-Tumor Effects of QDs-NGR Nanoparticles on Pancreatic Cancer Cells. *Sci. Adv. Mater.* **2021**, *13*, 2475–2482. [[CrossRef](#)]
56. He, Y.; Liu, Z.; Han, C.; Sun, S.-B.; Wu, Z.; Wang, J.-Y. A novel fast and sensitive fluorescent hydrogen sulfide probe with large stokes shift for imaging living cells and zebrafish. *J. Nanoelectron. Optoelectron.* **2022**, *17*, 516–524. [[CrossRef](#)]
57. Chaudhary, S.; Umar, A. Glycols functionalized fluorescent Eu₂O₃ nanoparticles: Functionalization effect on the structural and optical properties. *J. Alloy. Compd.* **2016**, *682*, 160–169. [[CrossRef](#)]

58. Zhang, L.; Wang, W.; Zhao, Y.; Zhao, F. Application of Fluorescent Nanoparticles in Immunodetection and Emergency Treatment of Myocardial Infarction Disease. *Sci. Adv. Mater.* **2021**, *13*, 1164–1171. [[CrossRef](#)]
59. Al-Hadeethi, Y.; Umar, A.; Al-Heniti, S.H.; Kumar, R.; Kim, S.H.; Zhang, X.; Raffah, B.M. 2D Sn-doped ZnO ultrathin nanosheet networks for enhanced acetone gas sensing application. *Ceram. Int.* **2017**, *43*, 2418–2423. [[CrossRef](#)]
60. Al-Hadeethi, Y.; Umar, A.; Ibrahim, A.A.; Al-Heniti, S.H.; Kumar, R.; Baskoutas, S.; Raffah, B.M. Synthesis, characterization and acetone gas sensing applications of Ag-doped ZnO nanoneedles. *Ceram. Int.* **2017**, *43*, 6765–6770. [[CrossRef](#)]
61. Gu, H.; Sun, C.; Wang, R.; Zhu, S.; Dong, Y.; Lv, R.; Huang, X.; Sun, Y.; Chen, Q. Metalloporphyrin-Based Fluorescent Sensor for the Discrimination of Volatile Organic Compounds Using Density Functional Theory. *J. Nanolectron. Optoelectron.* **2022**, *17*, 243–250. [[CrossRef](#)]
62. Chomba, H.; Pan, T.; Zhuo, X.; Zhao, L.; Wang, Y.; Huang, Z.; Martin, H.; Chen, D.; Nie, L. A Bio-Barcode Electrochemical DNA Biosensor Based on Poly T30 Copper Nanoparticle Signaling. *Sci. Adv. Mater.* **2021**, *13*, 73–79. [[CrossRef](#)]
63. Kumar, R.; Umar, A.; Chauhan, M.; Al-Hadeethi, Y. ZnO–SnO₂ nanocubes for fluorescence sensing and dye degradation applications. *Ceram. Int.* **2021**, *47*, 6201–6210. [[CrossRef](#)]
64. Yang, J.; Wang, Y.; Jin, X.-L.; Peng, Y.; Luo, J. Design and Fabrication of Near Ultraviolet Enhanced Composite Single Photon Avalanche Diode for Fluorescence Lifetime Imaging. *J. Nanolectron. Optoelectron.* **2022**, *17*, 267–274. [[CrossRef](#)]
65. Kumari, M.; Chaudhary, G.R.; Chaudhary, S.; Umar, A.; Akbar, S.; Baskoutas, S. Bio-Derived Fluorescent Carbon Dots: Synthesis, Properties and Applications. *Molecules* **2022**, *27*, 5329. [[CrossRef](#)] [[PubMed](#)]